

## Isentropic Analysis of a Simulated Hurricane

AGNIESZKA A. MROWIEC

*Center for Climate Systems Research, Columbia University, New York, New York*

OLIVIER M. PAULUIS

*Courant Institute of Mathematical Sciences, New York University, New York, New York, and Center for Prototype Climate Modeling, New York University Abu Dhabi, Abu Dhabi, United Arab Emirates*

FUQING ZHANG

*Department of Meteorology, The Pennsylvania State University, University Park, Pennsylvania*

(Manuscript received 2 March 2015, in final form 29 July 2015)

### ABSTRACT

Hurricanes, like many other atmospheric flows, are associated with turbulent motions over a wide range of scales. Here the authors adapt a new technique based on the isentropic analysis of convective motions to study the thermodynamic structure of the overturning circulation in hurricane simulations. This approach separates the vertical mass transport in terms of the equivalent potential temperature of air parcels. In doing so, one separates the rising air parcels at high entropy from the subsiding air at low entropy. This technique filters out oscillatory motions associated with gravity waves and separates convective overturning from the secondary circulation.

This approach is applied here to study the flow of an idealized hurricane simulation with the Weather Research and Forecasting (WRF) Model. The isentropic circulation for a hurricane exhibits similar characteristics to that of moist convection, with a maximum mass transport near the surface associated with a shallow convection and entrainment. There are also important differences. For instance, ascent in the eyewall can be readily identified in the isentropic analysis as an upward mass flux of air with unusually high equivalent potential temperature. The isentropic circulation is further compared here to the Eulerian secondary circulation of the simulated hurricane to show that the mass transport in the isentropic circulation is much larger than the one in secondary circulation. This difference can be directly attributed to the mass transport by convection in the outer rainband and confirms that, even for a strongly organized flow like a hurricane, most of the atmospheric overturning is tied to the smaller scales.

### 1. Introduction

Hurricanes develop through a complex interplay between dynamics and thermodynamics. The energy that powers them is gained at the surface through surface enthalpy fluxes and frictional heating. It is transported upward within the eyewall and lost to radiative cooling at the tropopause (e.g., [Bister and Emanuel 1998](#)). A fully developed tropical cyclone in a quasi-steady state can be approximated as axisymmetric vortices in which the flow

follows the constant angular momentum lines along constant entropy surfaces ([Emanuel 1986](#); [Emanuel and Rotunno 2011](#)). This type of approximation focuses on the eyewall circulation and the upper bound on the hurricane intensity as well as the analytical solution for the radial structure of such idealized tropical cyclone can be derived. While idealized conceptual models are able to reproduce a number of the large-scale features of mature tropical cyclones (such as maximum wind speed or thermodynamic structure) and thus offer important insights on the nature of hurricanes, the actual behavior of real storms is much more complex owing to a wide range of scales involved. For example, interactions between organized convection in spiral rainbands in the outer convective

---

*Corresponding author address:* Olivier Pauluis, CIMS, New York University, 251 Mercer Street, New York, NY 10012.  
E-mail: pauluis@cims.nyu.edu

regions and the eyewall can cause intensity variations and possibly play a role in the rapid intensification or the eyewall replacement cycle.

In the present study, we utilize the isentropic analysis technique recently developed by Pauluis and Mrowiec (2013, hereinafter PM13). This framework relies on sorting the vertical mass transport and other flow properties in terms of the equivalent potential temperature ( $\theta_e$ ) and is appropriate to study the atmospheric motions in high-resolution numerical simulations. Isentropic analysis of convective motions stems from the body of research initiated by Rossby (1937). It is analogous to the studies of meridional circulation and takes advantage of the fact that potential temperature and entropy are quasi conserved in the free troposphere. As shown in PM13, the equivalent potential temperature can be used to replace both horizontal coordinates at each level in the model so that the flow can be described using height and entropy ( $z-\theta_e$ ) as coordinates. This offers a straightforward way to identify the mean properties of rising and subsiding air parcels. Air parcels with similar thermodynamic properties can be followed in an averaged sense as they are carried by convective updrafts and downdrafts, and a mean isentropic overturning circulation can be computed.

In contrast to the disorganized radiative–convective equilibrium simulations studied in PM13, a hurricane exhibits a secondary circulation that organizes the convection. It will be shown here that the mass transport associated with the isentropic streamfunction is much larger than the secondary circulation. This situation is similar to the well-known difference between the Eulerian-mean meridional circulation and the isentropic circulation in the midlatitudes (Pauluis et al. 2008, 2010). For the meridional circulation, differences between the mass transport in either isentropic or Eulerian coordinates can be explained by the fact that the poleward eddy heat transport corresponds to a physical mass transport related to the Stokes drift of air parcels under the influence of the eddies (Pauluis et al. 2011). A similar situation arises here, with convective motions playing a similar role to that of midlatitude eddies. In particular, the isentropic mass transport can be decomposed between a contribution from the secondary circulation and a contribution from the convective scale, with the latter dominating the overall transport. This approach also makes it possible to unambiguously extract a convective mass transport in high-resolution simulations.

This paper is focused on applying the isentropic analysis to study the overturning occurring in a mature hurricane. It is organized as follows: Section 2 of the paper describes the numerical simulations. Section 3 presents a description of the isentropic analysis method, followed by its application in context of numerically resolved convection in a hurricane.

Section 4 discusses how the isentropic streamfunction can be decomposed into the contributions from the secondary circulation and from convection. It is then argued that convection is the dominant contribution to the atmospheric overturning, even in a mature hurricane like the one in our simulation. We then offer our summary and conclusions in section 5.

## 2. Hurricane simulations

### a. WRF Model setup

In this study, we apply isentropic analysis to an idealized hurricane simulation produced using the Weather Research and Forecasting (WRF) mesoscale numerical model with version 2.2 of the Advanced Research WRF dynamical solver (Skamarock et al. 2005) in a nested grid configuration. The model solves the compressible Navier–Stokes equations with Coriolis curvature terms (the simulation was performed on the  $\beta$  plane), uses a staggered Arakawa C-grid, and the prognostic variables are in a scalar-conserving flux form. It was initialized with an axisymmetric vortex similar to Rotunno and Emanuel (1987), located at 20°N with an initial radius of 102 km and tangential wind  $v_t = 16 \text{ m s}^{-1}$ . The temperature and humidity profiles follow Jordan (1958) soundings and there was no large-scale environmental flow. The longwave and the shortwave radiation heating are neglected as in Nolan (2007). This choice for the model setup prevents an unrealistic cooling of the upper troposphere during the initial phase of the simulations as it takes time for sufficient amount of convection to develop and balance radiative cooling. This also implies that, as the atmosphere slowly evolves toward thermal equilibrium in the absence of radiative forcing, the simulated hurricane will inevitably decay. The analysis here is based on a sequence of instantaneous snapshots taken every 6 min of the innermost domain which covers a 1000 km by 1000 km area with a 1-km horizontal resolution (Rozoff et al. 2012). There are 35 vertical levels with the top at 28 km, stretched from 0.6 km in the boundary layer to 3.6 km at the atmospheric top. For cloud microphysics, the WRF single-moment 6-class microphysics scheme (WSM6) with graupel is used (Hong et al. 2004), and the Yonsei University (YSU) scheme (Noh et al. 2003) is used for the representation of subgrid-scale turbulence. Because of the high horizontal resolution the convection is resolved explicitly; thus, there is no need for the cumulus parameterization.

### b. Temporal and spatial variability

The present study focuses on 2.5 days of a fully developed hurricane simulation previously analyzed by Fang and Zhang (2012) and Rozoff et al. (2012), corresponding

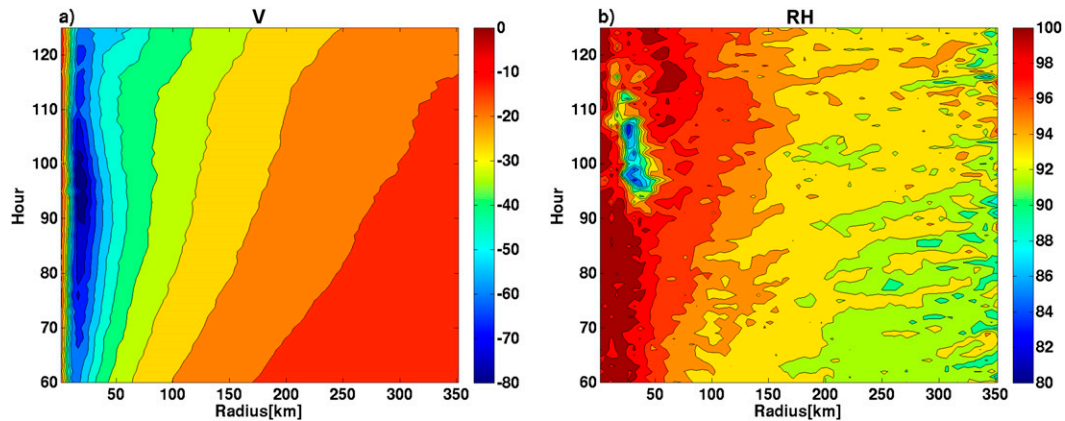


FIG. 1. (a) Tangential wind ( $\text{m s}^{-1}$ ) evolution at level of 1 km and (b) relative humidity (%) at the same level. Vertical axis is given in hours since the beginning of the run.

to the period in which the storm is most active between hours 60 to 126. The Hovmöller diagram of the azimuthally averaged tangential wind and relative humidity at the altitude of 500 m are shown in Figs. 1a and 1b, respectively. The simulated storm is well defined and its intensity (measured by the tangential wind speed) fluctuates through the simulation. It is the most intense between the hours 90 to about 102, with the tangential winds reaching  $80 \text{ m s}^{-1}$  at about 25 km from the center. Over the following 12 h the primary eyewall gradually weakens and past hour 114 the strong tangential winds expand horizontally. At that time the maximum tangential wind drops by about 25%. The weakening of the primary eyewall is followed by formation of a new balance for a wider vortex with a lower tangential wind (not shown here).

As can be seen in the relative humidity field Fig. 1b, there is a region of relatively dry air reaching the surface at hour 96, which indicates the formation of the downdrafts and cold pools—a direct consequence of reevaporation of precipitation falling outside the eyewall. The downdrafts bring cooler and drier air to the boundary layer, thus disrupting the inflow that fuels the eyewall. A secondary eyewall emerges at the edge of the cold pool and is associated with a secondary maximum in relative humidity. There is a 6-h delay between the formation of the cold pool and the weakening of the hurricane. This is roughly consistent with the time it takes to advect the cold pool into the eyewall. This evolution pattern is part of the eyewall replacement cycle as discussed by Fang and Zhang (2012) and Rozoff et al. (2012). The subsequent weakening of the storm is expected in our simulations as the absence of radiative cooling leads to a gradual warming of the entire troposphere.

In this study, we focus on hurricane evolution before the replacement cycle is completed. Based on the tangential

wind field, during the evolution of the storm the three stages of the evolution are distinguished:

- the intensification lasting about 30 h,
- a 12-h period of peak intensity (hours 90–102),
- and a 24-h long weakening.

These three stages are used here to compare the thermodynamics structure of the storm at these different points of its evolution. Unless stated otherwise, we focus on the quasi-steady, axisymmetric, peak intensity circulation and average the parameters of interest over that stage in the storm's evolution.

To further describe the storm, four fields averaged over the period of peak intensity are shown in Fig. 2 in the radial and vertical coordinates. The secondary circulation is captured by vertical and radial velocities (Figs. 2a and 2b, respectively): air flows toward the center near the surface, rises in the eyewall, and then moves away from the center in the upper troposphere. In addition, the vertical velocity field indicates the presence of a mesoscale downdraft at the outer edge of the eyewall (around 50 km). Farther away from the center, there is a broad ascent region.

The secondary circulation strongly affects the thermodynamic structure of the storm. The equivalent potential temperature is shown in Fig. 2c. Away from the center, the equivalent potential temperature exhibits a midtropospheric minimum at about 5 km, typical of tropical soundings. As one nears the center of the storm, the equivalent potential temperature in the inflow gradually increases, and the minimum of  $\theta_e$  moves closer to the surface. A mesoscale downdraft brings the cooler, drier air toward the surface, which shows up as intrusion of low  $\theta_e$  air at a radius of about 50 km. The inner and outer boundaries of the eyewall are captured by the slanted isentropic surfaces for

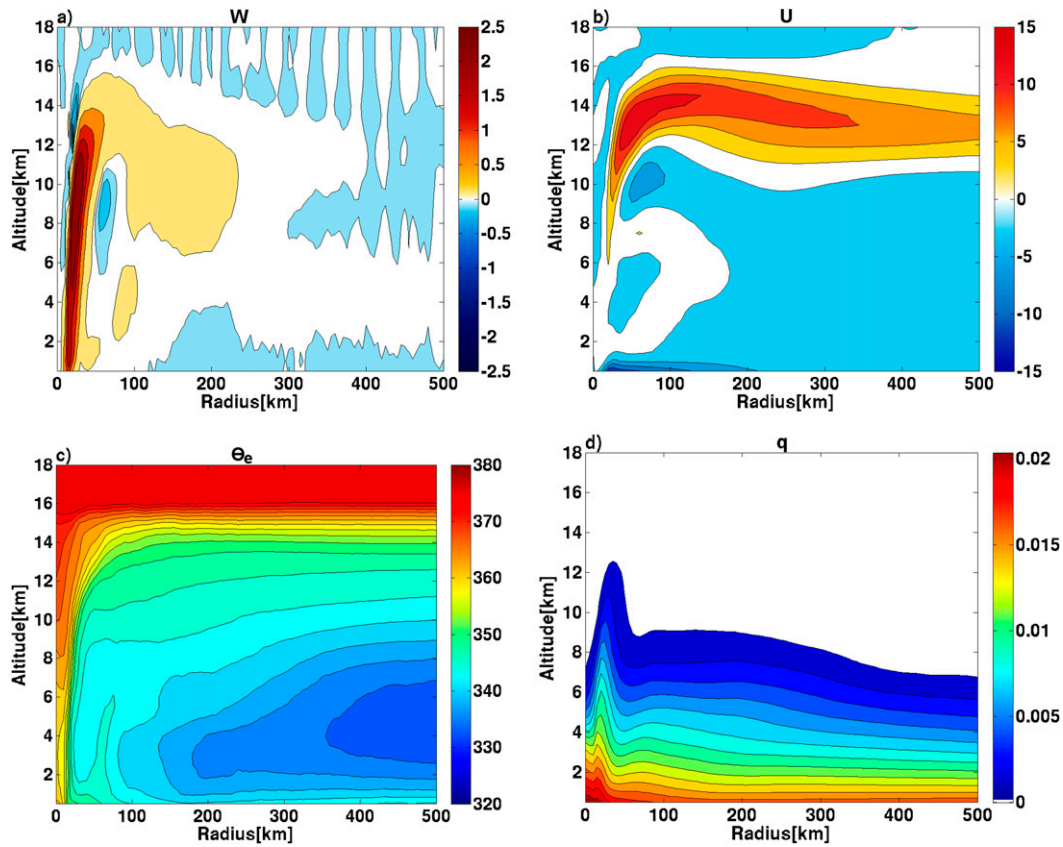


FIG. 2. (a) Vertical and (b) radial velocities ( $\text{m s}^{-1}$ ) make the secondary circulation. (c) Equivalent potential temperature (K) and (d) the total water mixing ratio ( $\text{g kg}^{-1}$ ) are shown. All fields are azimuthally and temporally averaged over the peak intensity period.

$\theta_e = 360 \text{ K}$  and  $\theta_e = 350 \text{ K}$ . These extend from the surface to the tropopause where they connect with to the upper-tropospheric outflow region. The total water mixing ratio field, shown in Fig. 2d, shows a gradual moistening of the inflow as it nears the center of the storm, with the eyewall clearly visible as a sharp maximum in water content. The water distribution also clearly indicates the eye, characterized by descending stratospheric air with high equivalent potential temperature and low water content.

### 3. Isentropic analysis

Isentropic surfaces are defined here as the surfaces of constant equivalent potential temperature ( $\theta_e$ ), which is conserved for reversible moist adiabatic processes. We use equivalent potential temperature following Emanuel [1994, his Eq. (4.5.11)] defined as

$$\theta_e = \frac{T}{\Pi} \mathcal{H}^{-(R_v r_v)/C} \exp\left(\frac{L_v r_v}{CT}\right),$$

where  $T$  is temperature,  $\Pi = (p/p_0)^{R_d/C}$  is the Exner function,  $p_0$  is the reference pressure, and  $R_v$  and  $R_d$  are

the gas constant of water vapor and dry air, respectively. The specific heat  $C$  is given by  $C = c_{pd} + c_l r_T$ , with  $c_{pd}$  and  $c_l$  as the specific heat at constant pressure of dry air and liquid water, respectively;  $L_v$  is the latent heat of vaporization;  $\mathcal{H}$  is the relative humidity; and  $r_v$  and  $r_T$  are, respectively, the mixing ratio for water vapor and total water (defined as water in all three phases). The equivalent potential temperature  $\theta_e$  is related to entropy of moist air as follows:

$$S = C \ln \frac{\theta_e}{T_{\text{ref}}},$$

with  $T_{\text{ref}}$  a reference temperature.

Figure 3 shows a snapshot of three isentropic surfaces from the simulation, corresponding to  $\theta_e = 360 \text{ K}$ ,  $350 \text{ K}$ , and  $340 \text{ K}$ . These values of  $\theta_e$  were chosen to emphasize various aspects of the hurricane circulation. The isosurface for  $\theta_e = 360 \text{ K}$  is shown in Fig. 3a. It is typically located in the upper levels of the troposphere. However, this isosurface here extends all the way to the sea level at the center. This isentropes corresponds to the upper value of  $\theta_e$  found in the eyewall and can be viewed as the

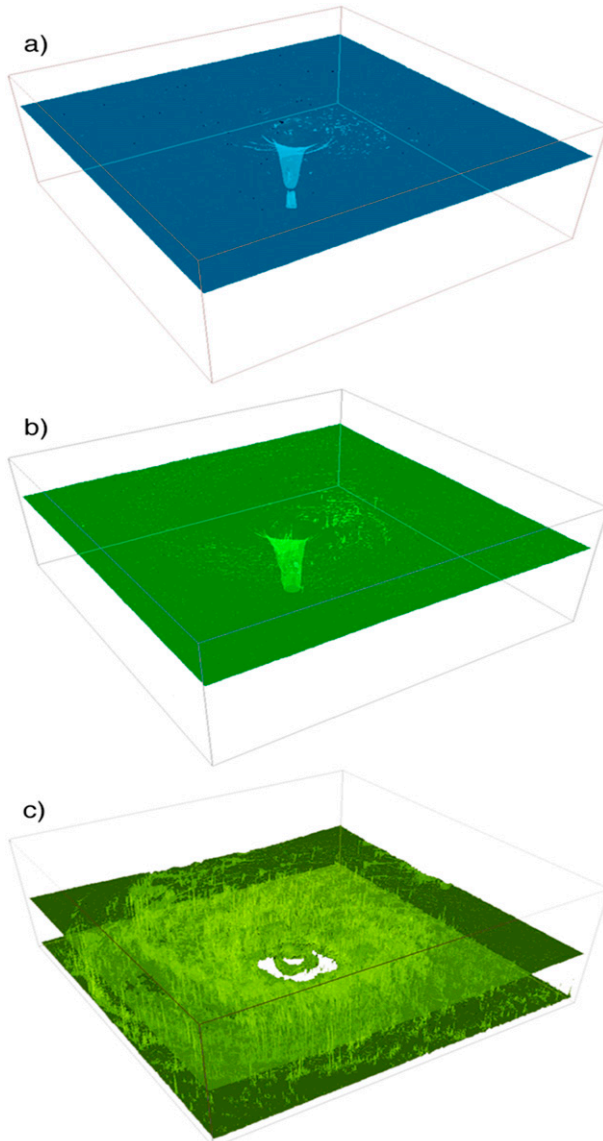


FIG. 3. Isentropic surfaces for three values of  $\Theta_e$ : (a) 360, (b) 350, and (c) 340 K.

inner boundary of the eyewall and upper boundary of the outflow. The value of 350 K in Fig. 3b corresponds to the lower value of  $\theta_e$  in the eyewall and marks the outer boundary of the eyewall and lower boundary of the outflow. Away from the eye, there are ripples on the isosurface (also to a lesser extent visible in Fig. 3a).

These ripples are the manifestations of propagating gravity waves induced by underlying convection. The isosurface for  $\theta_e$  of 340 K is shown in Fig. 3c. The geometry of the 340-K isosurface is very complex. First, it is folded into two main manifolds, one near the surface and one in the midtroposphere, corresponding approximately to the level where the horizontal mean equivalent potential temperature is equal to 340 K. Second, these two manifolds are connected through numerous intermittent isentropic tubes that correspond to the occurrence of deep convective updrafts that transport moist air from the boundary layer to the upper troposphere. These convective “tubes” occur preferentially within the outer rainbands, as expected from the rainfall distribution. One may also notice the presence of a number of smaller isentropic bubbles from the lower manifold that do not make it to the upper manifold. These would correspond either to congestus clouds, which dissipate before reaching the midtroposphere, or to developing convective cells. The structure of these isosurfaces thus points out to a thermodynamic distinction between the ascending air in the eyewall with  $350 < \theta_e < 360$  K and convection in the outer rainband associated with lower value of the equivalent potential temperature.

#### *Isentropic mass flux*

The isentropic surfaces shown in Figs. 3a–c are quite complicated and it would be very difficult to analyze the properties of the air parcels or to follow their individual trajectories. One way to overcome this problem is by sorting the air parcels according to their thermodynamic properties using the isentropic averaging proposed by PM13. This method takes advantage of the fact that, in moist convection, updrafts have a higher equivalent potential temperature than subsiding air. To do so, the properties of the flow at each level  $z$  are conditionally averaged on the equivalent potential temperature  $\theta_e$ . As a result, the two horizontal coordinates  $(x, y)$  are replaced by one thermodynamic coordinate ( $\theta_e$ ) while the dependence on altitude is retained.

The framework of PM13 here is modified to better take advantage of the structure of the storm and, in particular, of its dependence on the radius. We define an isentropic integral of a function  $f$  as the integral at a given vertical level on a given isentropic surface and radial ring:

$$\langle f \rangle(z, \theta_{e0}, r_0, t) = \iint_A f(x, y, z, t) \delta\{\theta_e - \theta_e(x, y, z, t)\} \delta\{r_0 - r(x, y)\} dx dy, \quad (1)$$

where  $\delta\{\cdot\}$  is the Dirac delta function and  $r$  is the distance to the center of the domain, which also

corresponds approximately to the center of the storm through the simulation. The horizontal integral is taken

over the domain  $A$ , which is a 1000 km by 1000 km square inner grid of the simulation. The integration radius  $r_0$  and equivalent potential temperature  $\theta_{e0}$  are treated as constant parameter on the right-hand side. This function is approximated by averaging  $f$  over the finite size  $\theta_e$  and  $r$  bins (1 K was used for  $\Delta\theta_e$  and 5 km for  $\Delta r$ ). Thus,  $\delta\{\theta_{e0} - \theta_e\} \sim 1/\Delta\theta_e$  and, by analogy,

$\delta\{r_0 - r\} \sim 1/\Delta r$ . This process is repeated at each time step and each vertical level, resulting in a distribution dependent on height, equivalent potential temperature, radial distance, and time.

Based on the integral definition Eq. (1), a joint distribution of the vertical mass flux in isentropic and radial coordinates  $\langle \rho w \rangle$  is constructed as follows:

$$\langle \rho w \rangle(z, \theta_{e0}, r_0, t) = \iint_A \rho(x, y, z, t) [w(x, y, z, t) - \bar{w}(z, t)] \delta\{\theta_{e0} - \theta_e(x, y, z, t)\} \delta\{r_0 - r(x, y)\} dx dy, \quad (2)$$

where  $\rho$  is the mass per unit volume,  $w$  is the vertical velocity, and  $\bar{w}(z, t)$  is the vertical velocity averaged over the entire domain  $A$ . Removing the mean vertical velocity is done here in order to define of the isentropic streamfunction as discussed in section 4. The regular units for the mass flux  $\rho w$  are kilograms per square meter per second ( $\text{kg m}^{-2} \text{s}^{-1}$ ). Note that, because of the conditional averaging over  $\theta_e$  and radial distance, the isentropic mass flux units are kilograms per second per meter per Kelvin ( $\text{kg s}^{-1} \text{m}^{-1} \text{K}^{-1}$ ).

The isentropic mass flux integrated over all radial distances over a time period  $P$  is given by

$$\langle \rho w \rangle_{\theta_e}(z, \theta_e) = \frac{1}{P} \int_0^P \int_0^\infty \langle \rho w \rangle(r', \theta_e, z, t') dr' dt'. \quad (3)$$

The units here are kilograms per second per Kelvin ( $\text{kg s}^{-1} \text{K}^{-1}$ ). The isentropic mass flux averaged over the peak intensity is shown in Fig. 4.

To understand how the isentropic mass flux relates to the physical space, it is convenient to look at it starting at the highest values of the equivalent potential temperature and move to the left of the scale. For  $380 > \theta_e > 360$  K, there is a downward mass flux that extends from the tropopause to the surface. As was shown in Fig. 2c, this range of  $\theta_e$  values is characteristic for the lower stratosphere and is also present within the eye of the hurricane. Thus, this corresponds to the downward mass flux of stratospheric air within the eye. Between 360 and 350 K the mass flux is positive and that marks the upward mass transport within the eyewall. The equivalent potential temperatures below 350 K are characterized by a strong mass transport in both directions. Warm, moist air is transported upward between 350 and 345 K and cooler, drier air descends at lower equivalent potential temperature. The mass transport is strongest in the lower troposphere, below 6 km. It may seem at first counterintuitive that the eyewall with the strongest mean vertical velocity has such weak mass transport, but as the area of eyewall is much smaller than that of the

outer region, its contribution is comparatively small. As we will discuss later, the isentropic mass transport is dominated by the convective scale.

The previous discussion suggests that the isentropic mass transport in the hurricane is also strongly tied to the organization of the storm. To further confirm this, we look at the spatial distribution of the mass transport for different  $\theta_e$  intervals. The mass flux (averaged over the peak intensity) in three thermodynamic regions of the storm isolated on the basis of the equivalent potential temperature intervals for the eye and the eyewall 348–368 K, updrafts 339–347 K, and cold large-scale downdrafts 323–338 K are shown in Figs. 5a–c, respectively. The eye and the eyewall occupy the high end of the equivalent potential temperatures, which quite distinctly isolate the upward mass transport in the eyewall and subsidence in the eye (Fig. 5a). For an intermediate value of  $\theta_e$ , we observe ascending motions below the freezing level through most of the domain, even in regions where the Eulerian-mean vertical velocity is downward (Fig. 2a). A second region of ascent is found in the upper troposphere at about 200 km from the center, which coincides with the region of mesoscale ascent of the outer rainband. In addition, there is a narrow region of downward motion located closer to the eyewall and some mid- to upper-troposphere subsidence far away from the storm center (Fig. 5b). Air at the low end of the equivalent potential temperature range is typically moving downward, especially in the lower troposphere (Fig. 5c). In the region between 100 and 350 km there is a strong cancellation between ascending air with  $339 \leq \theta_e \leq 347$  K and descending air with  $323 \leq \theta_e \leq 338$  K. This is a signature of convective overturning, with most of the convective motion concentrated below the melting level below 4 km [as also observed by Li and Wang (2012)].

Next, the simulation is time averaged over the three stages in the hurricane lifetime—intensification, peak intensity, and weakening—discussed in section 2. We further separate the isentropic mass transport between

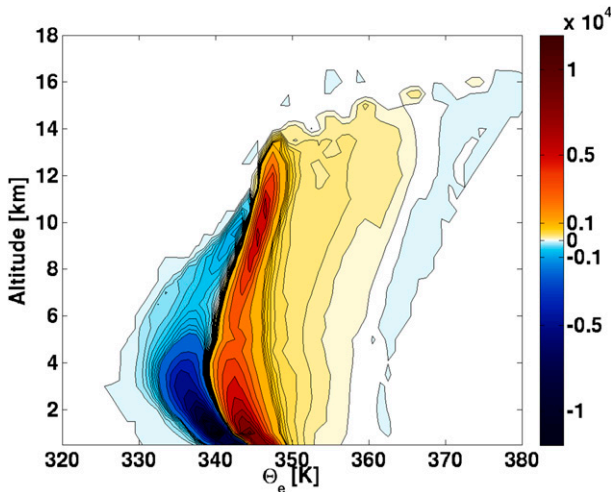


FIG. 4. Total domain isentropic mass flux ( $10^6 \text{ kg s}^{-1} \text{ K}^{-1}$ ) averaged over the peak intensity of the simulated hurricane.

the contribution from the inner region for the radial distance  $0 \leq r \leq 75 \text{ km}$  and the outer region with  $75 \leq r \leq 250 \text{ km}$ . The results for the three stages of the life cycle are shown in Fig. 6. The inner region encompasses both the eye and eyewall. In the intensification phase (Fig. 6a), the ascent in the eyewall takes place at equivalent potential temperature between 345 and 355 K. There is some downward mass flux at low level for  $z \leq 4 \text{ km}$  and low  $\theta_e < 340 \text{ K}$ . Subsidence within the eye appears as a downward mass transport of air with high value of  $\theta_e > 360 \text{ K}$ . As the hurricane reaches its peak intensity (Fig. 6c), the ascent in the eyewall circulation shifts toward higher values of  $\theta_e$ . Finally, as the primary eyewall weakens (Fig. 6e), there is also significantly less ascending motion with the inner region. In this respect, intensification is characterized by an increase of the equivalent potential temperature in the eyewall, while the weakening corresponds to a reduction in the upward mass flux.

The isentropic mass transport in the outer region is shown in Figs. 6b, 6d, and 6f. The difference in color scale used for the inner region (left column) and outer region (right column) should be noted: the isentropic mass transport in the outer region is one order magnitude greater than that in the inner region. The outer region is dominated by convection and the isentropic mass flux exhibits many similar characteristics to radiative convective equilibrium simulations discussed in PM13. In particular, the mass transport peaks near the lower boundary and the equivalent potential temperature of the ascending branch decreases in the lower troposphere as a result of entrainment. In the upper troposphere, the  $\theta_e$  of the ascending motion increases as a

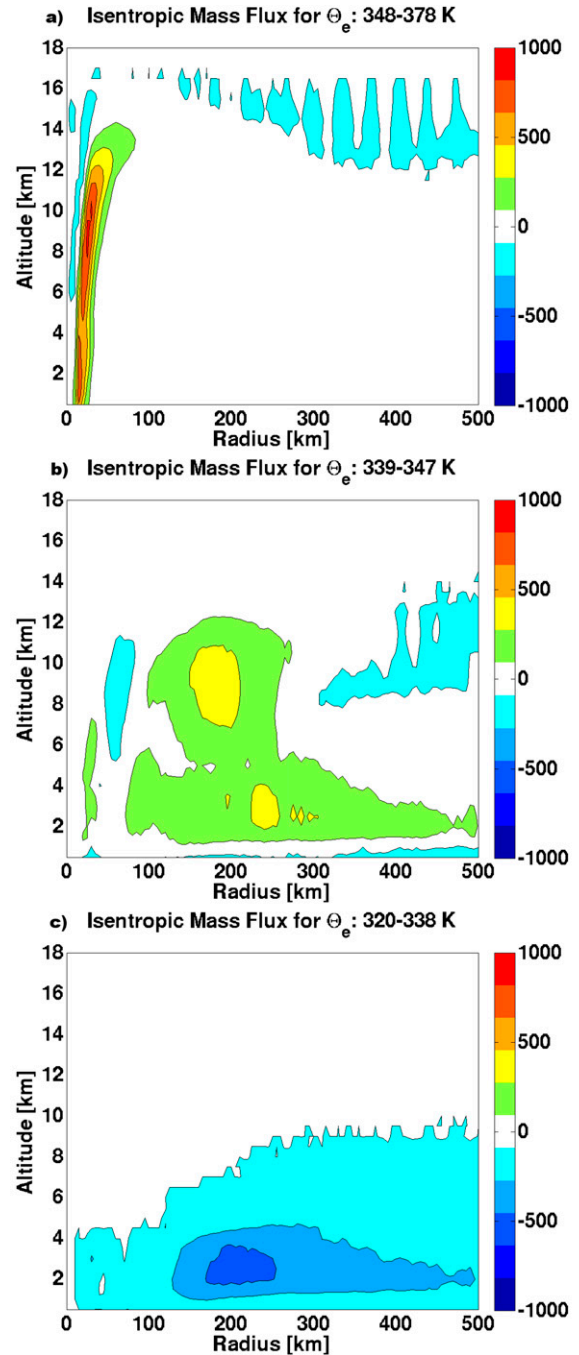


FIG. 5. Upward isentropic mass flux during the most intense period. Each plot shows mass flux per unit radius ( $10^3 \text{ kg s}^{-1} \text{ m}^{-1}$ ) averaged over different equivalent potential temperature ranges: (a)  $348 \leq \theta_e \leq 378 \text{ K}$ , (b)  $339 \leq \theta_e \leq 347 \text{ K}$ , and (c)  $320 \leq \theta_e \leq 338 \text{ K}$ .

result of freezing. The main difference with the simulations of PM13 lies in the presence of a secondary maximum of the mass transport in the upper troposphere. While changes in the storm intensity are reflected in the isentropic mass transport within the inner region, the

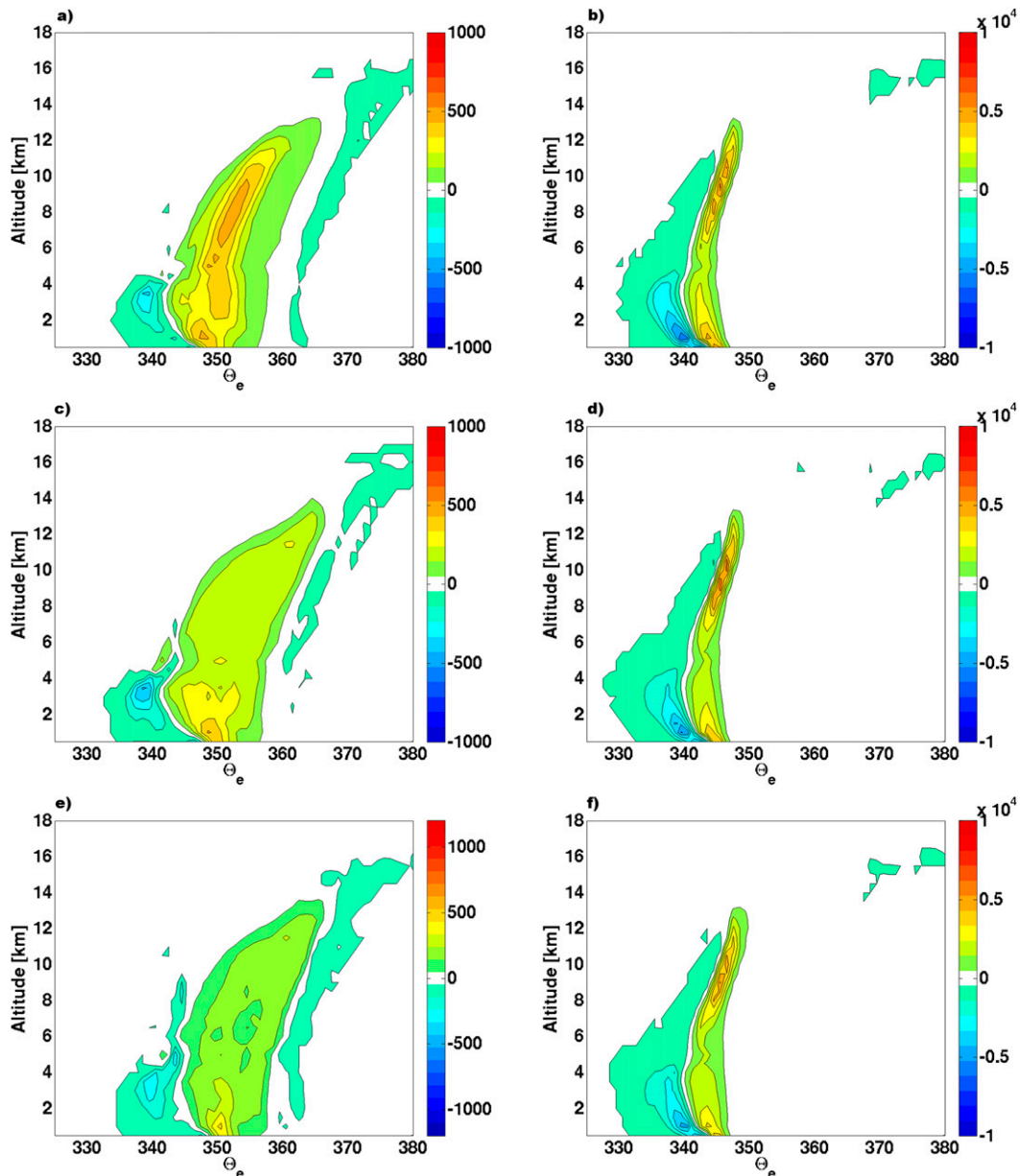


FIG. 6. Isentropic mass flux averaged ( $10^6 \text{ kg s}^{-1} \text{ K}^{-1}$ ) over different subdomains and different time periods. (left) Inner region for  $r < 75 \text{ km}$ . (right) Outer regions with  $75 < r < 250 \text{ km}$ . (top) Intensification period. (middle) Maximum intensity. (bottom) Weakening period.

isentropic mass transport in the outer region seems unaffected. The main evolution appears in a gradual shift toward warmer equivalent potential temperatures in the mass transport, which reflects the gradual warming of the domain in the absence of radiative cooling.

#### 4. Isentropic and Eulerian mass transports

The mass flux defined by Eq. (2) can be integrated to obtain the isentropic streamfunction

$$\Psi_{\theta_e}(\theta_e, z, t) = \int_0^{\theta_e} \int_0^{\infty} \langle \rho w \rangle dr d\theta'_e, \quad (4)$$

which offers a very useful and relatively simple illustration of the convective flow. Note that in order for the streamfunction to vanish at large  $\theta_e$ , there cannot be any net upward mass transport at that level. Alternatively, one can subtract the domain-averaged vertical velocity from the computation of the isentropic mass flux, as it has been done here [see Eq. (3)]. The isentropic

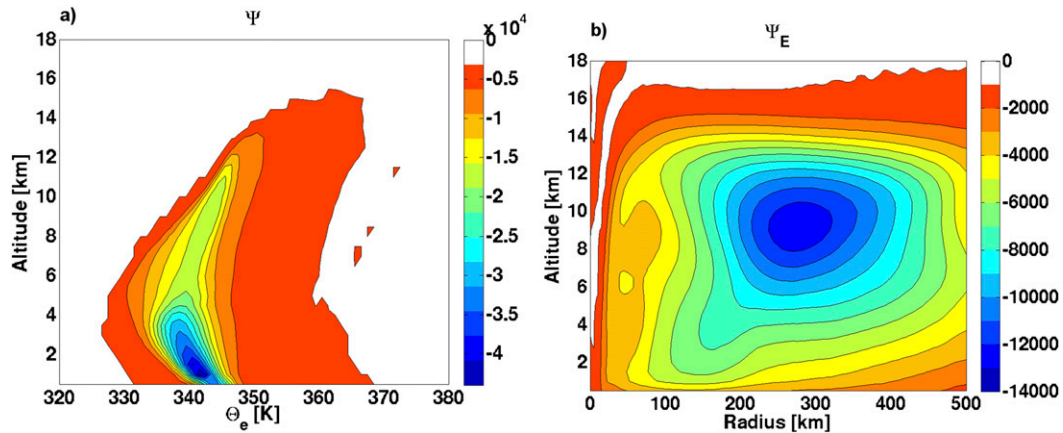


FIG. 7. Comparison of the (a) isentropic and (b) Eulerian streamfunctions ( $10^6 \text{ kg s}^{-1}$ ).

streamfunction is equal to the total upward mass transport of all air parcels with an equivalent potential temperature less than a given  $\theta_e$  at each vertical level and at each time step. As was shown in PM13 (their section 4), for a steady flow, the vertical derivative of the streamfunction is proportional to the mean diabatic tendency, and contours of constant value of the streamfunction can be interpreted as the mean trajectories of air parcels in this thermodynamic space  $z-\theta_e$ . Note that these are not trajectories of individual air parcels but rather the averaged trajectories of all the parcels with similar thermodynamic properties.

The time-averaged isentropic streamfunction is shown in Fig. 7a. The minimum near the surface indicates that the vertical mass transport is dominated by shallow convection. The air parcels are transported upward along the streamlines from the surface up at the high end of the equivalent potential temperatures. As they ascend, their  $\theta_e$  value is not exactly conserved. It decreases from the surface to the melting level (at 5 km) as a result of mixing and entrainment and increases slightly along the streamlines above as freezing leads to a slight increase in  $\theta_e$ . Past the apex point, the air parcels move downward and the equivalent potential temperature decreases. The lowest values of the equivalent potential temperature are found at the melting level. Below the freezing level, the equivalent potential temperature of descending air parcels gradually increases as they gain water vapor detrained from clouds.

Analogously to the isentropic counterparts, an Eulerian streamfunction can be defined as

$$\Psi_E(z, r, t) = 2\pi r \int_0^z [\rho v] dz', \quad (5)$$

where  $v$  is the radial velocity and the brackets denote azimuthal averaging. The Eulerian streamfunction is thus equal to the net outward mass transport between

the surface and height  $z$  at a distance  $r$  from the center of the domain. For a steady flow, it also corresponds to the net downward mass flux at level  $z$  and at a distance less than  $r$  from the center of the domain and can also be obtained from the vertical velocity field:

$$\begin{aligned} \Psi_E(z, r, t) &= - \int_0^r 2\pi r' [\rho w] dr' \\ &= - \int_0^r \int_0^\infty \langle \rho w \rangle d\theta'_e dr'. \end{aligned} \quad (6)$$

The Eulerian streamfunction is shown in Fig. 7b. The minimum value of this streamfunction is located at the level of about 9 km and at about 300 km away from the storm's center. As was shown in Fig. 2b, the inflow layer in this simulation is relatively deep, which explains that the minimum of the Eulerian streamfunction is located in the upper troposphere.

The amplitude of the minimum of the Eulerian and isentropic streamfunctions can be viewed as a mass transport by the residual circulation. It is thus interesting to compare the difference in strength and vertical location of the Eulerian and isentropic mass transports. The mass transport in isentropic coordinate is about three times as strong as the Eulerian mass transport. The former also peaks near the surface, while the latter is located in the upper troposphere. Even at its peak value, the Eulerian streamfunction  $\Psi_E$  is still weaker than the minimum value of isentropic streamfunction  $\Psi$  at the same level.

Such differences between the Eulerian and isentropic descriptions of the same hurricane flow are similar to the differences that exist when the global atmospheric circulation is averaged in either Eulerian coordinates or isentropic coordinates. In the former, air velocity is averaged on the constant pressure levels and results in the classic three-cell structure for each hemisphere. Alternatively, air velocity may be averaged on the constant

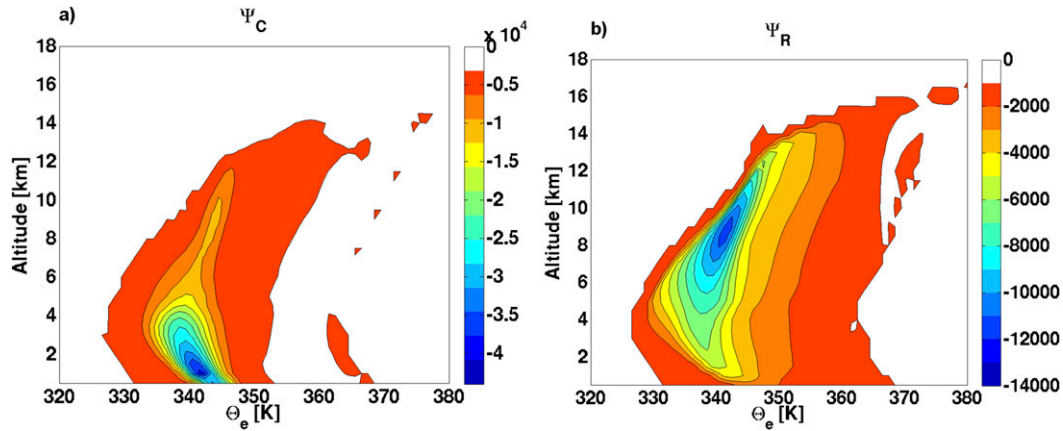


FIG. 8. Decomposition of the isentropic streamfunction between contributions from (a) convection  $\Psi_C$  and (b) from the secondary circulation  $\Psi_R$  ( $10^6 \text{ kg s}^{-1}$ ). See text for details.

potential temperature levels like, for example, in [Held and Schneider \(1999\)](#) or [Pauluis et al. \(2008, 2010\)](#). In this case there is only one overturning cell per hemisphere observed. These differences between the Eulerian and isentropic representations arise from the fact that synoptic eddies, which are associated with a meridional energy transport in Eulerian coordinates, correspond to a net mass transport in isentropic coordinates. In the case of the hurricane, convection plays the role of the synoptic eddies for the global circulation: under an Eulerian averaging, convective motions are associated with a zero net mass flux but a net upward energy transport. Under an isentropic averaging, the upward energy transport is turned into an upward mass flux of air at high  $\theta_e$  balanced by a downward mass transport of air at lower  $\theta_e$ . One thus expects a significant contribution of the convective scales to the isentropic circulation whenever convection contributes significantly to the upward energy transport.

To further confirm this interpretation, we decompose the isentropic mass flux between a mean and a convective contribution:

$$\langle \rho w \rangle = \langle \rho \rangle [w] + \langle \rho w' \rangle, \quad (7)$$

where  $[w]$  is the azimuthal mean vertical velocity and  $w' = w - [w]$  is the departure from the azimuthal mean flow. This decomposition of the vertical velocity can be used to similarly decompose the streamfunction:

$$\underbrace{\int_0^{\theta_e} \int_0^{\infty} \langle \rho w \rangle dr' d\theta'_e}_{\Psi} = \underbrace{\int_0^{\theta_e} \int_0^{\infty} \langle \rho w' \rangle dr' d\theta'_e}_{\Psi_C} + \underbrace{\int_0^{\theta_e} \int_0^{\infty} \langle \rho \rangle [w] dr' d\theta'_e}_{\Psi_R}. \quad (8)$$

The first integral on the right-hand side corresponds to the azimuthal eddy contribution to the streamfunction. Here, the eddy corresponds primarily to variations in the vertical velocity associated with convection, albeit  $\Psi_C$  is computed using the departure of the vertical velocity from the azimuthal mean and thus includes contributions from a variety of scales such as vortex Rossby waves or asymmetric rainband. The second term on the right-hand side corresponds to the contribution from the azimuthal mean (secondary) circulation. Both components of resulting streamfunction decomposition are shown in [Figs. 8a and 8b](#). The isentropic convective streamfunction is of the same magnitude as the total streamfunction in [Fig. 7a](#) and recovers most of the shallow overturning convection. The streamfunction associated with the secondary circulation ([Fig. 8b](#)) is much weaker than the convective component. Its amplitude is of the same magnitude as the Eulerian streamfunction shown in [Fig. 7b](#) and occurs at the same level.

To further confirm that the isentropic streamfunction associated with the azimuthal mean flow ( $\Psi_R$ ) indeed corresponds to the secondary circulation, we show how it can be fairly well approximated by the Eulerian streamfunction. The underlying idea of this reconstruction is that almost everywhere in the hurricane the equivalent potential temperature at a given height decreases with the distance from the center of the storm. This is not true for the locations of the strong downdrafts, but for the sake of the approximation we can define  $[\theta_e](z, r)$  as the azimuthal mean equivalent potential temperature and invert it at constant height to find  $r_{\theta_e}(z, \theta_e)$  the radius at which the equivalent potential temperature is equal to  $\theta_e$ . Then, we can project the Eulerian streamfunction  $\Psi_E$  into  $z$ - $\theta_e$  coordinates as  $\Psi_E\{z, r_{\theta_e}(z, \theta_e), z\}$ .

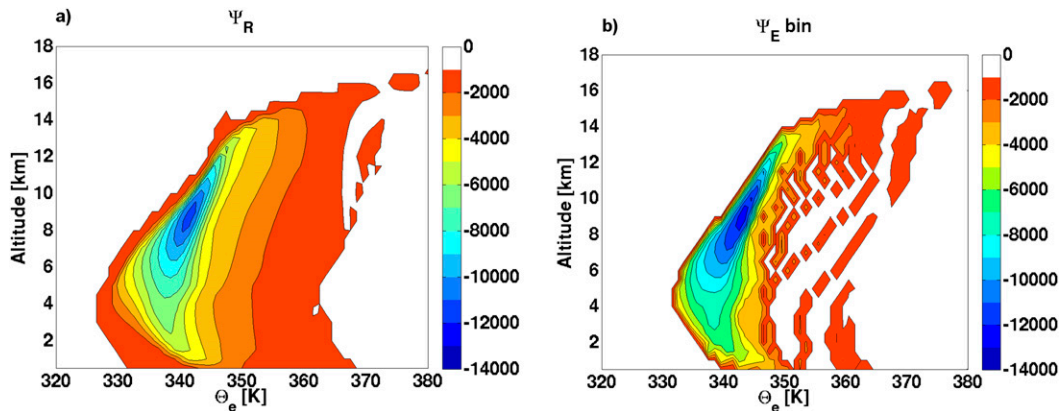


FIG. 9. Contribution of (a) the secondary circulation to the isentropic streamfunction  $\Psi_R$  and (b) its approximation based on the Eulerian streamfunction ( $10^6 \text{ kg s}^{-1} \text{ K}^{-1}$ ). See text for details.

Figure 9 compares the isentropic streamfunction associated with the secondary circulation  $\Psi_R$  (Fig. 9a) to the Eulerian streamfunction projected into the  $z$ – $\theta_e$  coordinates (Fig. 9b). Because the relationship between  $r$  and  $\theta_e$  is not exactly monotonic, there are bound to be some differences. For example,  $\Psi_E$  bin is narrower, especially at the low end of the equivalent potential temperature scale, which shows that some downdrafts are missing in the reconstruction. The high end of the  $\theta_e$  scale is also different, most likely because of the radius–equivalent potential temperature transformation. However, despite these differences, the reconstructed field is very similar to the residual overturning

$$\Psi_R(z, \theta_e) \approx \Psi_E\{z, r_\theta(z, \theta_e)\}.$$

The isentropic streamfunction captures the overall overturning associated with the hurricane. It can be decomposed into a contribution from the secondary circulation and a contribution from convection (here more loosely defined as departure from azimuthal average). The contribution from the secondary circulation is small—about one-third of the total. This indicates that the overturning in our simulations remains primarily driven at the convective scales. In other words, the secondary circulation acts primarily to spatially reorganize the convective mass transport but does little to increase the overall mass transport in our simulation.

We will argue now that the mass transport by the convective scale has in fact to be significantly larger than the secondary circulation itself. Consider the inflow of the hurricane as shown by the Eulerian circulation in Fig. 7b. It is fairly deep, extending up to 8 km, and its equivalent potential temperature is quite low, between 330 and 335 K (as shown in Fig. 2c and Fig. 8b). As the air gets closer to the center of the storm, its  $\theta_e$  gradually

increases until it reaches a value between 345 and 350 K and is ready to rise in the upper troposphere (the small fraction of the inflow that makes it to the eyewall is further heated to  $\theta_e \approx 360$  K). Most of the inflow is not in direct contact with the ocean and only gains energy from mixing with detraining clouds. A close look at the convective streamfunction in Fig. 8a shows that a typical updraft has a  $\theta_e$  of about 345 K while downdrafts occur at  $\theta_e \approx 340$  K. The increase of the equivalent potential temperature in the inflow by about 15 K occurs through multiple mixing events where the difference of  $\theta_e$  between updrafts and downdrafts is only 5 K. Conservation of energy requires the mass transport by these successive convective overturnings to be three times larger than the mass transport in the inflow. The core of this argument is twofold: First, while the hurricane is primarily driven by surface energy flux, the secondary circulation peaks away from the surface and must be heated through convective mixing. Second, the increase of  $\theta_e$  in the inflow is much larger than the variations of  $\theta_e$  in convective system. Together, these imply that the convective mass transport will be significantly larger than the secondary circulation.

This argument could be made more quantitative by considering the partitioning of the upward transport of equivalent potential between the secondary circulation and the eddies. The total vertical transport of  $\theta_e$  is equal to minus the integral of the isentropic streamfunction:

$$\begin{aligned} F(z) &= \frac{1}{P} \iiint_A \rho w \theta_e \, dx \, dy \, dt \\ &= -\frac{1}{P} \int_0^P \int_0^\infty \Psi_{\theta_e}(\theta'_e, z, t) \, d\theta'_e \, dt. \end{aligned} \quad (9)$$

At low level, say at the cloud base  $z_{CB}$ , this transport is dominated by the convective scale, and we have

$$\begin{aligned}
 F(z_{CB}) &= -\frac{1}{P} \int_0^P \int_0^\infty \Psi_C(\theta'_e, z_{CB}, t) d\theta'_e dt \\
 &= \Delta\Psi_C \Delta\theta_{e,C}.
 \end{aligned} \tag{10}$$

Here,  $\Delta\Psi_C$  is the mass transport by the convective scale (defined as the difference between the maximum and minimum of the streamfunction  $\Psi_C$  at the cloud base) and  $\Delta\theta_{e,C}$  is the difference of equivalent potential temperature between rising and subsiding air. It is defined through Eq. (10) and corresponds qualitatively to the width of the streamfunction in Fig. 8a.

Consider now the equivalent potential temperature transport at level  $z_E \approx 8$  km where the Eulerian streamfunction reaches its peak amplitude. The total transport of  $\theta_e$  at this level will be larger than the transport due to residual circulation:

$$\begin{aligned}
 F(z_E) &\geq -\frac{1}{P} \int_0^P \int_0^\infty \Psi_R(\theta'_e, z, t) d\theta'_e dt \\
 &= \Delta\Psi_R \Delta\theta_{e,R}.
 \end{aligned} \tag{11}$$

The inequality here is due to the fact that the convective transport is not negligible. In this expression,  $\Delta\Psi_E$  is the mass transport by the secondary circulation and  $\Delta\theta_{e,R}$  is the difference of enthalpy between the ascending and descending branch of the secondary circulation. In the absence of an energy source within the free troposphere, the vertical transport of  $\theta_e$  decreases with height, so that we have

$$F(z_{CB}) > F(z_E).$$

But then, Eqs. (10) and (11) yield

$$\Delta\Psi_R \leq \frac{\Delta\theta_{e,C}}{\Delta\theta_{e,R}} \Delta\Psi_C. \tag{12}$$

This indicates that the convective mass transport will be at least as large as the mass transport of the secondary circulation multiplied by the ratio of the variations of  $\theta_e$ . In our simulation, the variations of  $\theta_e$  at the convective scale to be smaller than the difference of  $\theta_e$  between the eyewall and the free troposphere away from the storm. One thus expects that the mass transport at the convective scale to be significantly larger than the mass transport by the secondary circulation, in good agreement with the isentropic analysis presented here.

The fact that the mass transport by the secondary circulation is weaker than that by the smaller atmospheric scales does not mean that the secondary circulation does not have an important impact of the flow. A valid interpretation of the constraint [(12)] is that a

given large-scale flow is able to modulate the spatial distribution of a much larger convective mass transport. Furthermore, the secondary circulation in our simulation contributes significantly to the mass transport in the upper troposphere, where its impact is comparable to that of the convective scales in our simulation. The secondary circulation may thus have a significant role in controlling the depth of the atmospheric overturning.

## 5. Conclusions

In this paper we applied a new analysis technique developed in PM13 to an idealized three-dimensional hurricane simulation. The method is based on the conditional averaging of the mass transport with respect to the equivalent potential temperature. This thermodynamic averaging naturally separates warm and moist updrafts from colder and drier downdrafts and is well suited for studying convective motions in high-resolution simulations. While PM13 apply the isentropic analysis to look at the behavior of convection in radiative–convective equilibrium, the present study looks at the isentropic circulation in an idealized hurricane in which convection strongly interacted with the secondary circulation.

The upward mass transport exhibits both some strong similarities and differences with that obtained by PM13 for disorganized convection. As for convection, the flow is characterized by ascending air at high value of  $\theta_e$  and descending air at low value of  $\theta_e$ . The mass transport is maximum near the surface, indicative of the important role played by shallow convection. Furthermore, the equivalent potential temperature of the ascending air decreases with height, which is a signature of the entrainment of dry air into the updrafts. The isentropic circulation in the hurricane case also exhibits some noticeable difference from that of convection. First, there is a small but significant ascent of air with very high  $\theta_e$  (with  $350 \leq \theta_e \leq 360$  K) that corresponds to the ascending motion within the eyewall. While clearly detectable in the isentropic analysis, this ascent only accounts for a small fraction of the total isentropic mass transport. Second, subsidence within the eyewall can also be observed and is associated with the downward motion of stratospheric air with very high equivalent potential temperature (with  $\theta_e \geq 360$  K).

While the flow within the eye and eyewall can be clearly identified in the isentropic analysis, the bulk of the mass transport is tied to convective motions outside the radius of maximum wind. In our simulation, most of the upward motion takes place at intermediate value of the equivalent potential temperature (with

$340 \leq \theta_e \leq 350$  K) between 150 and 300 km away from the storm center. Similarly, the subsidence is associated with low entropy air (with  $\theta_e \leq 340$  K) and occurs over a broad portion of the domain. Scattered convection in the outer regions dominates the mass transport, in large part because of the fact that it occupies a much larger area than the eyewall itself.

The isentropic circulations for three different stages of the storm have also been compared. It is found that the changes in the intensity are mostly reflected in the change in the isentropic mass transport in the inner region. In particular, the period of peak intensity is characterized by a strong ascent in the eyewall that also occurs at a significantly larger equivalent potential temperature. This would indicate that achieving much higher value of  $\theta_e$  in the eyewall is an important aspect of hurricane intensity, which is in good agreement with thermodynamic theory for hurricane intensity (Emanuel 1986; Emanuel and Rotunno 2011). In contrast, there is little change in the isentropic flow in the outer regions. This suggests that convection outside of the eyewall acts primarily as a sort of thermodynamic bath that indirectly controls the hurricane intensity but that is, in itself, weakly affected by the internal dynamics of the storm center.

The isentropic circulation can also be compared to the mass transport by the secondary circulation. This can be readily achieved by comparing the isentropic streamfunction in  $\theta_e, z$  coordinates [(4)] to the Eulerian streamfunction in  $r, z$  coordinates [(6)]. The isentropic streamfunction can be interpreted as the net upward mass flux at a given level of all air parcels with an equivalent potential temperature less than a given threshold. Similarly, the Eulerian streamfunction is given by the net upward mass flux at a given level of all air parcels within a certain distance from the center of the storm. Our analysis shows that the isentropic streamfunction is an order of magnitude larger than the Eulerian streamfunction. The former also peaks near the surface, while the latter has a minimum in the upper troposphere.

The difference in mass transport between the Eulerian and isentropic averaging is a direct consequence of how convective mass transport is treated by these two averaging procedures. On the one hand, as long as the upward mass transport in the updraft is balanced by an equal downward mass flux in the downdraft at the same distance from the storm center, the two mass fluxes will cancel out when averaging in Eulerian coordinates. On the other hand, updrafts occur at a larger value of  $\theta_e$  than the downdraft. As a result, the mass flux in the updraft and downdraft is accounted for at a distinct value of  $\theta_e$  when analyzing the flow in isentropic coordinates. We

have shown here how that isentropic streamfunction can indeed be decomposed between a contribution from the convective scale and a contribution from the secondary circulation, with the latter being directly related to the Eulerian-mean circulation. In our simulation, the contribution from the convective scale dominates the total mass transport, with the secondary circulation accounting only for a small fraction of the mass transport.

The fact that the overturning circulation is dominated by the convective scale is an important limitation of analyzing the circulation obtained from coarse-resolution datasets or models. Indeed, coarse-resolution models or datasets that exclude the convective scale only capture the atmospheric overturning by the large-scale atmospheric motion. As such, they miss the contribution from smaller scales—including convection—which account for most of the vertical mass transport. In particular, Lagrangian trajectories reconstructed from coarse-resolution datasets are not representative of parcel trajectories in regions of active convection. A direct application of the isentropic analysis lies in its ability to objectively extract overturning simulations, which can then be compared between models with different resolution or physical representation.

In our study, we have emphasized the fact that hurricanes are complex flow in which convection and the flow at larger-scale continuously interact. The isentropic analysis for convective motions initially introduced in PM13 offers a new way to look at such complex flows by sorting out the mass transport in terms of the thermodynamic properties of the air parcels. It is particularly well suited for studying overturning circulation in high-resolution simulations. A key result here is to show that even for highly organized flow such as a hurricane, the upward mass transport is dominated by the convective scale, while the secondary circulation contributes primarily through a slight deepening of the overturning, but otherwise does not lead to any significant increase in the overall mass transport. Any understanding of the dynamics of hurricanes must address the nature of its interactions with convection.

*Acknowledgments.* Agnieszka Mrowiec is supported by the DOE Office of Science, Office of Biological and Environmental Research, through Contract DE-PS02-09ER09-01. Olivier Pauluis is supported by the New York University in Abu Dhabi Research Institute under Grant G1102. Fuqing Zhang is supported by the Office of Naval Research Grant N000140910526 and NASA Grant NNX12AJ79G.

## REFERENCES

- Bister, M., and K. A. Emanuel, 1998: Dissipative heating and hurricane intensity. *Meteor. Atmos. Phys.*, **65**, 233–240, doi:[10.1007/BF01030791](https://doi.org/10.1007/BF01030791).
- Emanuel, K. A., 1986: An air–sea interaction theory for tropical cyclones. Part I: Steady-state maintenance. *J. Atmos. Sci.*, **43**, 585–604, doi:[10.1175/1520-0469\(1986\)043<0585:AASITF>2.0.CO;2](https://doi.org/10.1175/1520-0469(1986)043<0585:AASITF>2.0.CO;2).
- , 1994: *Atmospheric Convection*. Oxford University Press, 580 pp.
- , and R. Rotunno, 2011: Self-stratification of tropical cyclone outflow. Part I: Implications for storm structure. *J. Atmos. Sci.*, **68**, 2236–2249, doi:[10.1175/JAS-D-10-05024.1](https://doi.org/10.1175/JAS-D-10-05024.1).
- Fang, J., and F. Zhang, 2012: Effect of beta shear on simulated tropical cyclones. *Mon. Wea. Rev.*, **140**, 3327–3346, doi:[10.1175/MWR-D-10-05021.1](https://doi.org/10.1175/MWR-D-10-05021.1).
- Held, I. M., and T. Schneider, 1999: The surface branch of the zonally averaged mass transport circulation in the troposphere. *J. Atmos. Sci.*, **56**, 1688–1697, doi:[10.1175/1520-0469\(1999\)056<1688:TSBOTZ>2.0.CO;2](https://doi.org/10.1175/1520-0469(1999)056<1688:TSBOTZ>2.0.CO;2).
- Hong, S.-Y., J. Dudhia, and S.-H. Chen, 2004: A revised approach to ice microphysical processes for the bulk parameterization of clouds and precipitation. *Mon. Wea. Rev.*, **132**, 103–120, doi:[10.1175/1520-0493\(2004\)132<0103:ARATIM>2.0.CO;2](https://doi.org/10.1175/1520-0493(2004)132<0103:ARATIM>2.0.CO;2).
- Jordan, C. L., 1958: Mean soundings for the West Indies area. *J. Meteor.*, **15**, 91–97, doi:[10.1175/1520-0469\(1958\)015<0091:MSFTWI>2.0.CO;2](https://doi.org/10.1175/1520-0469(1958)015<0091:MSFTWI>2.0.CO;2).
- Li, Q.-Q., and Y. Wang, 2012: Formation and quasi-periodic behavior of outer spiral rainbands in a numerically simulated tropical cyclone. *J. Atmos. Sci.*, **69**, 997–1020, doi:[10.1175/2011JAS3690.1](https://doi.org/10.1175/2011JAS3690.1).
- Noh, Y., W.-G. Cheon, S.-Y. Hong, and S. Raasch, 2003: Improvement of the *K*-profile model for the planetary boundary layer based on large eddy simulation data. *Bound.-Layer Meteor.*, **107**, 401–427, doi:[10.1023/A:1022146015946](https://doi.org/10.1023/A:1022146015946).
- Nolan, D. S., 2007: What is the trigger for tropical cyclogenesis? *Aust. Meteor. Mag.*, **56**, 241–266.
- Pauluis, O. M., and A. A. Mrowiec, 2013: Isentropic analysis of convective motions. *J. Atmos. Sci.*, **70**, 3673–3688, doi:[10.1175/JAS-D-12-0205.1](https://doi.org/10.1175/JAS-D-12-0205.1).
- , A. Czaja, and R. Korty, 2008: The global atmospheric circulation on moist isentropes. *Science*, **321**, 1075–1078, doi:[10.1126/science.1159649](https://doi.org/10.1126/science.1159649).
- , —, and —, 2010: The global atmospheric circulation in moist isentropic coordinates. *J. Climate*, **23**, 3077–3093, doi:[10.1175/2009JCLI2789.1](https://doi.org/10.1175/2009JCLI2789.1).
- , T. Shaw, and F. Laliberte, 2011: A statistical generalization of the transformed Eulerian-mean circulation for an arbitrary vertical coordinate system. *J. Atmos. Sci.*, **68**, 1766–1783, doi:[10.1175/2011JAS3711.1](https://doi.org/10.1175/2011JAS3711.1).
- Rossby, C.-G., 1937: Isentropic analysis. *Bull. Amer. Meteor. Soc.*, **18**, 201–209.
- Rotunno, R., and K. A. Emanuel, 1987: An air–sea interaction theory for tropical cyclones. Part II: Evolutionary study using a nonhydrostatic axisymmetric numerical model. *J. Atmos. Sci.*, **44**, 542–561, doi:[10.1175/1520-0469\(1987\)044<0542:AAITFT>2.0.CO;2](https://doi.org/10.1175/1520-0469(1987)044<0542:AAITFT>2.0.CO;2).
- Rozoff, C. M., D. S. Nolan, J. P. Kossin, F. Zhang, and J. Fang, 2012: The roles of an expanding wind field and inertial stability in tropical cyclone secondary eyewall formation. *J. Atmos. Sci.*, **69**, 2621–2643, doi:[10.1175/JAS-D-11-0326.1](https://doi.org/10.1175/JAS-D-11-0326.1).
- Skamarock, W. C., J. B. Klemp, J. Dudhia, D. O. Gill, D. M. Barker, W. Wang, and J. G. Powers, 2005: A description of the advanced research WRF version 2. NCAR Tech. Note NCAR/TN-468+STR, 88 pp., doi:[10.5065/D6DZ069T](https://doi.org/10.5065/D6DZ069T).